Nanoscale

PAPER

View Article Online
View Journal

Cite this: DOI: 10.1039/d6nr00391e

Synergistic ruthenium single-atom and nanoparticles in nickel as cooperative catalysts for the alkaline hydrogen evolution reaction

Gaëlle Khalil,[a] Marie-Sophie Dias-Fernandes,[b,c] Sumit Bawari,[d] Linghui Li,[a,b] Chiddharth Muthuraj,[a] Florent Ducrozet,[e] Minkyoung Kwak,[f] Miguel Comesaña-Hermo, [a] Andrea Zitolo, [c] Stephan N. Steinmann, [d] Shannon W. Boettcher, [f] Cédric Tard, [b] Benedikt Lassalle-Kaiser, [c] Marion Giraud*[a] and Jennifer Peron *[a]

Efficient hydrogen evolution reaction (HER) catalysts that reduce the use of noble metals and can be synthesized on a large scale are essential for advancing anion exchange membrane water electrolyzers (AEMWEs) toward commercialization. Herein, we present a composite catalyst in which Ru nanoparticles coexist with Ru single-atom alloys (SAAs) dispersed within Ni nanoparticles (Ru-SAA/Ni), creating a highly active HER electrocatalyst. Using a one-pot and scalable synthesis method, we can tune the material composition from SAA, *i.e.* materials containing atomically dispersed Ru atoms (with ≤0.4 at% Ru) to composite structures in which SAAs coexist with Ru NPs. Comprehensive characterization using XPS, XAS, and TEM confirms Ru-SAA formation at a low Ru content and composite structures at higher contents. Electrochemical evaluations conducted in a three-electrode setup reveal that Ru-SAA/Ni composites achieve HER performance on par with that of Pt/C. Computational insights suggest that water dissociation is significantly faster at the Ru/Ni interface compared with that on extended surfaces. These active sites are thermodynamically as active as basal planes, preventing the excessive accumulation of reaction intermediates (H*, OH*). All these results highlight the synergistic interaction between Ru SAAs and Ru nanoparticles and their potential for large-scale applications with minimal use of precious metals. Finally, the materials are processed and tested in AEMWEs, achieving 1.85 V at 0.5 A cm^{-2} with a total noble metal loading of only 0.1 mg cm^{-2}.

Received 28th January 2026,
Accepted 16th March 2026

DOI: 10.1039/d6nr00391e

rsc.li/nanoscale

Introduction

To enable a sustainable future for humankind, there is an urgent need to develop large-scale, long-term green hydrogen production methods. Amongst carbon-free technologies, alkaline water electrolysis and proton exchange membrane water electrolysis will help meet this challenge.[1] However, for the mid- to long-term use of hydrogen and its widespread adoption across society, cost-effective production methods are required. In this context, anion exchange membrane water electrolyzers (AEMWEs) have emerged as a promising alternative. However, significant improvements in different cell components, such as membranes, ionomers and catalysts, are still required to bring this technology to a large-scale commercial level.[1–3] One of the main advantages of working under alkaline conditions is the ability to use non-noble metals as electrocatalysts, mostly due to the higher stability of first-row transition metals at high pH values. However, not only does the oxygen evolution reaction (OER) present sluggish kinetics but under alkaline conditions, the hydrogen evolution reaction (HER) is also associated with non-negligible overpotentials, thereby increasing the overall cost of H_2 production. In particular, it is now well established that under alkaline conditions, the HER is significantly slower than its acidic counterpart, even when using noble-metal catalysts.[4] The underlying causes of this phenomenon are still a matter of extensive research.[2,5]

In alkaline media, the HER is believed to proceed through a two-step reaction mechanism. In the first step (Volmer step), the water molecule is dissociated to form an adsorbed H

[a]*Université de Paris, CNRS, ITODYS, F-75013 Paris, France. E-mail: jennifer.peron@u-paris.fr, marion.giraud@u-paris.fr*
[b]*Laboratoire de Chimie Moléculaire (LCM), CNRS, École Polytechnique, Institut Polytechnique de Paris, 91120 Palaiseau, France*
[c]*Synchrotron SOLEIL, l'Orme des Merisiers, Départementale 128, 91190 Saint-Aubin, France*
[d]*CNRS, ENS de Lyon, UMR 5182, Laboratoire de Chimie, F69342 Lyon, France*
[e]*Sorbonne Université, Collège de France, CNRS, Laboratoire Chimie de la Matière Condensée de Paris (LCMCP), F-75005 Paris, France*
[f]*Department of Chemical & Biomolecular Engineering and Department of Chemistry, University of California, Berkeley, CA 94720, USA*

species (H*), while in the second step, this H* recombines either with another H* (Tafel step) or with an H atom directly provided by an adjacent water molecule (Heyrovsky step). Key factors to consider include intermediate adsorption energy, hydrogen binding energy, the presence of hydroxyl ions (OH^-), and the cation associated with OH^- in the electrolyte. These complex interactions, as well as the pH-dependent nature of the surfaces of the catalysts, remain major areas of research for improving the HER efficiency in alkaline media.[6] Recent studies have shown that the synergistic combination of two materials is a promising strategy to enhance the efficiency of this two-step, two-electron transfer process. A pioneering study by Markovic and coworkers[7] on heterofunctional catalysts based on the deposition of $Ni(OH)_2$ nanoparticles onto Pt surfaces has inspired further research. In this case, the $Ni(OH)_2$ nanoparticles are thought to activate the Volmer water dissociation step. Significant subsequent efforts have been dedicated to reducing the overpotential associated with the HER in alkaline media by intimately associating two different components at the nanometer scale.[8]

In recent years, the degree of complexity has increased, highlighting the synergistic effects associated with the use of composite materials made of metallic nanoparticles associated with single-atom catalysts (SACs). These materials hold the potential of pushing even further the limits of catalysis[9] and electrocatalysis.[10] In particular, Ru nanoparticles in combination with a SAC on carbon[11] or on oxide/hydroxide matrices[12] have shown exceptional performance towards the HER under alkaline conditions. Nevertheless, such multifunctional composites are often obtained through multistep and tedious synthetic procedures. Moreover, the electrochemical performances reported are achieved mostly in three-electrode electrochemical setups in 1 M KOH and not in full electrolysis devices. Such characteristics render the vast majority of materials reported in recent literature unlikely to be compatible with large-scale applications. Nickel-based electrocatalysts are promising candidates for achieving a performance comparable to that of precious metals, owing to the platinum-like electronic structure of nickel. Different strategies are currently being pursued to enhance its performance, including alloying or surface engineering.[13,14] For instance, the combination of Ni and Ru atoms has been identified as a promising composition to lower the kinetic barrier associated with water dissociation. However, the optimal material configuration (*i.e.* core@shell, alloy,[15] heterostructures[16] or SACs) has not yet been clearly established. For instance, Ruck and colleagues reported a single cell performance in 1 M KOH of 1.73 V at 1 A cm^{-2} with only 0.05 mg cm^{-2} of Ru, using highly dispersed Ni_{Ru} electrocatalysts on a carbon support, obtained through a two-step process involving a galvanic displacement reaction.[17]

Going beyond the mere synthesis of the catalyst and considering the integration of the materials into AEMWE devices, the chosen candidate should be processed into a catalytic layer from a catalyst ink to be deposited onto carbon substrates. Indeed, traditional metal foams used in liquid AWE are not ideal for membrane–electrode assembly configurations. For instance, the macroporous structure of these foams limits the electrode surface area in direct contact with the membrane, in opposition to the micro-porous structuration traditionally used with carbon-based diffusion layers. Additionally, the stiffness of the foam can easily induce the formation of pinholes in anion exchange membranes due to their inferior mechanical properties compared to proton exchange membranes. The poorer electrochemical performances of non-noble catalysts and/or the challenges in preparing catalyst nanoparticles that can be easily processed into catalyst layers mean that high noble metal loadings are still required at both the anode and cathode of AEMWE cells to achieve the best performance under alkaline conditions. Finally, in order to decrease the balance of plant and facilitate water and gas management, AEMWEs should operate with pure water or low electrolyte concentrations. However, the low overpotentials and favorable Tafel slopes reported in recent studies have mainly been achieved in experiments using at least 1 M KOH solutions. As a result, developing highly conducting solid electrolytes and catalysts with high activity in mild electrolyte concentrations is essential for making AEMWE devices more scalable and practical.

In this work, we employ a one-pot, single-step and scalable solution synthesis method to prepare a nanocomposite catalyst, in which Ru single atoms are effectively dispersed onto Ni particles. Additionally, a second family of catalysts, in which Ru–Ni structures are decorated with small Ru nanoparticles, has been developed using the same approach by simply increasing the noble metal content. Given that the same method is used to prepare all the nanocomposite materials presented herein, we are able to decouple the effect of the synthetic procedure from the final composition and performance of the material. Using a comprehensive set of characterization techniques, we demonstrate the synergistic effect of the combined Ru single atoms with Ru nanoparticles when both species are deposited on Ni. This allows us to achieve high performances with an ultralow noble metal loading of 0.1 mg cm^{-2} in AEMWE single cells in a 0.1 M KOH solution.

Experimental

Materials synthesis

Ruthenium(III) chloride hydrate (99.9%, $RuCl_3{\cdot}xH_2O$), nickel(II) acetate tetrahydrate (98%, $Ni(OAc)_2{\cdot}4H_2O$), and 1,2-butanediol (98%) were purchased from Sigma-Aldrich. Sodium hydroxide micro pearls were purchased from Thermo Fisher Scientific. All the chemicals were used as received, without further purification. In a one-pot synthesis, 0.08 M $Ni(OAc)_2{\cdot}4H_2O$, 0.08 M NaOH, and the desired amount of $RuCl_3{\cdot}xH_2O$ (with a Ru/(Ru + Ni) ratio between 0.5 and 10%) in 50 mL of 1,2-butanediol are mechanically stirred for 30 min at room temperature. The solution is then heated to 170 °C at a heating rate of 10 °C min^{-1}, and the reaction is kept at 170 °C for 90 min. Afterward, the reaction medium is cooled naturally to room temperature. Then, the nanoparticles are collected by centrifu-

gation at 20 000 rpm for 15 min and finally washed three times with 100% ethanol.

Scanning electron microscopy (SEM)

SEM experiments were performed using a ZEISS Gemini SEM 360 equipped with an Oxford Instruments Ultim Max 170 mm^2 detector. SEM images were obtained using an In-lens SE detector (In Column) at a 5 kV accelerating voltage.

Transmission electron microscopy (TEM)

TEM analyses were carried out using a JEOL 2100 FEG S/TEM microscope operated at 200 kV equipped with a spherical aberration probe corrector. Before analysis, the samples were dispersed in ethanol and deposited on a holey carbon-coated TEM grid.

X-ray diffraction (XRD)

XRD measurements were carried out using a PANalytical X'pert Pro diffractometer equipped with a Co anode (λ Kα = 1.79031 Å) and a multichannel X'Celerator detector. All the diffractograms were fitted with the MAUD program (Material Analysis Using Diffraction), a general X-ray diffraction program based mainly on the Rietveld refinement method, allowing the determination of the *a* and *c* parameters as well as the calculated crystallite sizes for each diffraction peak.

Energy dispersive X-ray fluorescence (EDXRF)

The elemental analyses of the powders were conducted by EDXRF using an epsilon 3XL spectrometer from PANalytical equipped with a silver X-ray tube. The calibration was performed by depositing a mass in the range of 5–20 μg of the standard solution of each element onto a polycarbonate membrane. The same conditions were adopted for all samples. The detection limits for Ru and Ni were determined to be 30 and 10 ng, respectively.

X-ray photoelectron spectroscopy (XPS)

XPS spectra were recorded using a K-Alpha+ spectrometer from Thermo Fisher Scientific, fitted with a microfocused, monochromatic Al Kα X-ray source ($h\nu$ = 1486.6 eV; spot size = 400 μm). The pass energy was set at 150 and 40 eV for the survey and narrow regions, respectively. Spectral calibration was determined by setting the main C 1s (C–C, C–H) component at 285 eV.

Physisorption

Physisorption studies were performed with N_2 at 77 K using a BELSORP-max apparatus from MicrotracBEL. Before analysis, the samples were outgassed at 423 K for 12 h under 0.1 Pa. BET isotherm studies were carried out in the relative pressure range of 0.05–0.25 Pa.

Electrochemical characterization

The potentiostat used for cyclic voltammetry was an Autolab PGSTAT12, and ohmic drop was compensated for in all cases (typically 30 Ω). The working electrode was a 5 mm-diameter glassy carbon rotating disk electrode (Metrohm Instrument), carefully polished and ultrasonically rinsed in absolute ethanol before use. The counter electrode was a graphite bar, and the reference electrode was a Hg/HgO electrode of 0.1 M KOH internal electrolyte. All the experiments were carried out in air at 10 mV s^{-1} and at a rotating rate of 1600 rpm. A 0.1 mol L^{-1} potassium hydroxide solution (99.99%, Sigma Aldrich) was used as a supporting electrolyte. From a mixture of 1 mg of the synthesized material, 2 mg of carbon Vulcan XC72R (Cabot), 25 μL of Nafion solution (5% w/w, Alfa Aesar), 100 μL of isopropanol (>99.5%, Sigma Aldrich) and 250 μL of deionized water (0.059 μS cm^{-2}), 8 μL of this suspension was deposited onto the electrode surface, which was then dried in air and left for 30 min at 60 °C in an oven. The catalysts were then subjected to 50 cycles in the capacitive region, between 0.1 and 0.5 V *vs.* RHE at 200 mV s^{-1}, and the 50th forward scan recorded at 10 mV s^{-1} in 0.1 M KOH M is presented. To accurately determine the Tafel slope for the hydrogen evolution reaction (HER) in alkaline media, linear sweep voltammetry (LSV) was performed at 0.01 V s^{-1}. The Tafel slope was then computed over a small range of potential (10 mV) to identify the regions where it remains constant, as described by Koper's group.[18]

In electrolysis cell testing

MEAs were prepared using a 40 μm-thick PiperION membrane. The membrane was cleaned overnight and stored in a 1 M KOH solution. Catalyst inks were prepared using 100 mg of catalyst: Co_3O_4 from US Nano at the anode and Pt/C or Ni_{Ru} + carbon black at the cathode, using 0.5 mL and 1.7 mL of isopropanol solution, respectively, with 200 mg of a 5 wt% PiperION (Versogen) dispersion. The solution was then sprayed onto a stainless steel fiber paper gas diffusion layer (Dioxide Materials) to reach a loading of 2.25 mg cm^{-2} at the anode and onto a Toray paper 090 gas diffusion layer to reach the desired loading at the cathode. A subsequent PiperION ionomer dispersion, diluted in ethanol, was sprayed onto the gas diffusion layers prior to assembly with the membrane. The MEA was then assembled in a 1 cm^2 cell and tested using a Biologic potentiostat connected to a homemade test station. Heated electrolyte was flowed on both the anode and cathode sides. The electrolyte temperature was set 5 K higher than the cell temperature (55 and 50 °C, respectively).

X-ray absorption spectroscopy

X-ray absorption spectroscopy measurements were carried out on the SAMBA beamline of Synchrotron SOLEIL and collected with a Si(220) double crystal monochromator (DCM) at an electron energy of 2.75 GeV. The energy was calibrated at the Ru (22 117 eV) and Ni (8333 eV) K-edges using ruthenium and nickel foils. The transmission mode was used to probe the material's structure as pellets, under *ex situ* conditions. Solid samples were prepared by mixing the catalyst and carbon black at a ratio of 5 : 95 and pressing them into 1.0 cm-diameter pellets. Acquisitions were done with 3 scans of 10 min each, within energy ranges of 22.0–23.3 keV

(dt = 0.05) and 8.2–9.5 keV (dt = 0.2) for the Ru and Ni K-edges, respectively.

Operando XAS experiments

Operando XAS experiments were performed in a three-electrode cell composed of an alkaline-proof Ag/AgCl reference electrode (E = 0.200 V) and graphite sheets (25 μm thickness) as the working and counter electrodes placed in a homemade cell. The catalytic ink was prepared by mixing 1 mg of catalyst and 2 mg of carbon black with 250 μL of Nafion solution (Nafion D-520 dispersion, 5% w/w in water and 1-propanol) and 250 μL of DI water solution. Then, 40 μL of this catalytic ink was deposited on the graphite foil and subsequently dried at room temperature first, and then at 60 °C for 30 min. After assembly, the cell was filled with a 0.1 M KOH solution (pH = 13) flowing at 1.7 mL min^{-1} to avoid bubble formation. Cyclic voltammetry (CV) and constant potential electrolysis (CPE) procedures were performed using a BioLogic SP-300 potentiostat. Ni and Ru K-edge *in situ*/*operando* X-ray absorption spectra were collected in the fluorescence mode using a 36-pixel, 30-element Ge detector (Canberra) at a 45° outgoing angle. The incoming photon intensity was monitored using a N_2/He-filled ionization chamber.

XAS data analysis

XANES and EXAFS data were processed using the Athena and Artemis softwares, respectively. For the XANES processing, consecutive scans were merged, and the edge position E0 was calibrated using the maximum of the first derivative peak of the XANES spectrum. The pre-edge and post-edge were subtracted from the background, and the edge-jump of the final spectrum was normalized to 1. Edge energy shifts are measured at half-edge jump intensity (normalized intensity = 0.5).

For the EXAFS, the k-range was set from 3 to 10.5 $Å^{-1}$ at the Ru K-edge and 3 to 12 $Å^{-1}$ at the Ni K-edge. Fourier transform EXAFS curve fitting was performed with Artemis using an *ab initio* FEFF calculation.[19] Fitting parameters are calculated using the EXAFS eqn (1) in the FEFF codes.

$$\chi(k) = {S_0}^2 \sum_j \frac{N_j}{kR_j^2} f_{\mathrm{eff}_j}(\pi, k, R_j) e^{-2\sigma_j^2 k^2} e^{-\frac{2R_j}{\lambda_j(k)}} \times \sin\left[2kR_j + \phi_{ij}(k)\right]. \quad (1)$$

In the equation, the parameters are defined for a given path R_j, which corresponds to the distance between the center atom and its neighboring atoms in the j shell. The coordination number N_j is the number of neighboring atoms in the j shell, and $f_{\mathrm{eff},j}(\pi, k, R_j)$ is the effective scattering amplitude. The Debye–Waller term, $e^{-2\sigma^2 k^2}$, describes the thermal and structural disorder in the path lengths R_j, while the mean free path λ_k and amplitude reduction factor ${S_0}^2$ are both related to the inelastic interactions.

For the FT-EXAFS analysis at the ruthenium K-edge, the ${S_0}^2$ factor was fixed to 0.72, according to the fit results of the Ru foil reference. The N, R and Debye–Waller factor (σ^2) fitting parameters were calculated using known structures of metallic Ru and RuO_2,[20] and an optimized structure of RuNi.

Density functional theory (DFT) computations

DFT computations were carried out in VASP 5.4.1[21] (Vienna *Ab initio* Simulation Package). Plane wave, spin-polarised orbitals with an energy cutoff of 500 eV describe the valence orbitals, and the PAW (Projector Augmented Wave)[22] formalism represents the valence–core interactions. The PBE (Perdew–Burke–Ernzerhof) exchange correlation functional[23] is used, and vdW interactions are corrected using the dDsC dispersion correction.[24] A Monkhorst–Pack 3 × 3 × 1 k-grid mesh is applied for all calculations. For solvation and the grand canonical DFT (GC-DFT) potential, an implicit solvent (size parameters of K+) is applied using VASPSol++.[25] In GC-DFT, the surface charge is varied and compensated for by the implicit solvent, and the electrode potential with respect to the standard hydrogen electrode (SHE) is calculated based on the Fermi energy of the surface at different applied charges. These discrete points are then fitted to a parabola for a continuous description of the energy as a function of the electrochemical potential, and a pH of 14 was used for converting the potential to RHE.

Results and discussion

The catalysts were obtained in a single step, using the polyol process.[26] To achieve this, $RuCl_3{\cdot}xH_2O$ was dissolved in 1,2-butanediol along with $Ni(OAc)_2{\cdot}4H_2O$ (Fig. 1a) owing to the high dielectric constant of the diol solvent. The reaction mixture was then heated to 170 °C to reduce the metal salts and obtain highly crystalline materials without any further thermal treatment.[26] The goal of this approach is to minimize the use of noble metal, while still optimizing the HER performance. The initial atomic ratio was varied from 0.5 to 10 Ru at% (relative to the total Ru + Ni content), and the structure, morphology, and chemical compositions of both the bulk and surface of the materials were systematically characterized. It should be noted that each synthesis was performed at least three times (up to ten times for the materials prepared with 2.5 Ru at%) to obtain *ca.* 230 mg of catalyst per batch. The yield of the reaction (based on the amount of solid material recovered after washing and drying overnight under vacuum) was found to be 95% ± 4%. The polyol process is known to be a scalable synthesis process, and the synthesis of the material prepared with 2.5 Ru at% was scaled up to 1 g without noticeable modification in the physico-chemical properties of the material.

Regardless of the initial Ru content introduced in the initial synthesis medium, the morphology of the particles is similar and consists of platelets forming aggregates of *ca.* 100 to 200 nm. A representative SEM image is shown in Fig. 1b. The Ru at% in the final material was assessed by X-ray fluorescence (XRF), and the actual Ru content compared to the Ru at% initially introduced in the synthesis media is plotted in Fig. 1c. The total Ru concentration in the final material

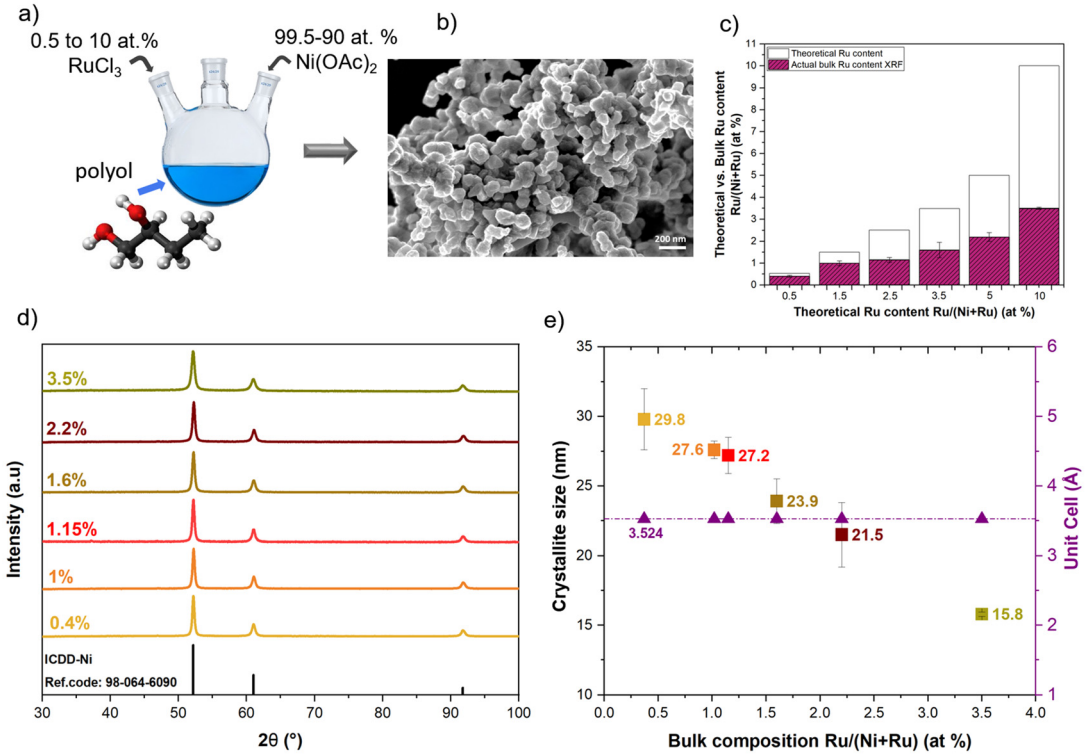

Fig. 1 (a) Schematic of the synthesis. (b) Representative SEM micrograph of Ni_{Ru} particles ($Ni_{Ru\ 1.15}$ in this case). (c) Ru at% determined from XRF measurements as a function of the initial Ru content in the solution. Results are averaged from at least three different syntheses. (d) X-ray diffractograms and (e) crystallite size and *a* cell parameter of Ni_{Ru} particles as a function of the initial Ru content in the synthesis. This content was determined from XRF measurements. The error bars represent the standard deviation calculated from measurements of at least three different syntheses.

increases from 0.4 to 3.5 at% as the initial Ru content in the solution is increased from 0.5% to 10%. The partial loss of Ru is attributed to the formation of ultrasmall Ru nanoparticles that are washed out during the centrifugation steps. The Ru at% determined from XRF measurements is used to label the samples (*i.e.* $Ni_{Ru\ 1.5\%}$ for a sample with 1.5 Ru at%). From the X-ray diffractogram presented in Fig. 1d, only one single face-centered cubic (fcc) crystalline phase characteristic of pure Ni is observed, regardless of the Ru content. The crystallite size and cell parameters were determined using Rietveld refinement (Fig. 1e), showing that the crystalline domain size decreases as the Ru content in the initial solution increases. Thus, the crystallite size is 29.8 nm for $Ni_{Ru\ 0.4\%}$ and decreases to 15.8 nm for $Ni_{Ru\ 3.5\%}$. Importantly, the cell parameter value (a = 3.52 Å) remains constant regardless of the Ru content, demonstrating that the bulk structure of the Ni particles is similar to that of pure Ni.

Further characterization of the bulk and surface composition of the samples was conducted using X-ray photoelectron spectroscopy (XPS), high-resolution transmission electron microscopy (HRTEM), and X-ray absorption spectroscopy (XAS). The X-ray absorption near-edge spectra (XANES) of the Ni_{Ru} particles at the Ni K-edge overlap with the spectrum of the nickel foil, indicating that, regardless of the Ru content, the particles are essentially composed of metallic Ni (Fig. S1). This is in agreement with the crystalline structure determined by XRD. However, XPS analysis in the Ni 2p region shows the presence of peaks characteristic of both Ni(0) with the 2p3/2 and 2p1/2 located at 852.7 and 970.1 eV, respectively, and oxidized Ni species with broader peaks at slightly higher binding energies (Fig. S2). Ni particles are easily prone to oxidation upon exposure to air and humidity, but, owing to the overlapping peaks characteristic of the different phases of hydroxylated and oxidized Ni particles, it is challenging to determine an exact composition for the oxidized layer at the surface of the objects. However, we can conclude that the oxidized layer is thin enough (<2 nm) for metallic Ni to be detected by XPS.[27]

Unlike Ni, both the XPS spectra in the Ru region and the XAS spectra recorded at the Ru K-edge exhibit a clear evolution with the Ru content in the material. As shown in Fig. 2a, the final Ru concentration determined by XPS increases with the initial amount introduced in the synthesis, but to a much greater extent than the Ru content measured by XRF. While XRF measures the atomic composition of the entire material, XPS is surface-sensitive, primarily probing the first 2 nm of the nanoparticle surface. For instance, the sample with a bulk Ru content of 0.4 at% shows a surface concentration of 3.2 at%. Similarly, when the bulk content is 2.2 at%, the surface Ru content determined by XPS increases to 25%. Accordingly, XPS measurements clearly indicate that Ru is mostly located at the surface of the objects. For each sample, the Ru XPS signal was fitted to determine its oxidation state at the surface of the par-

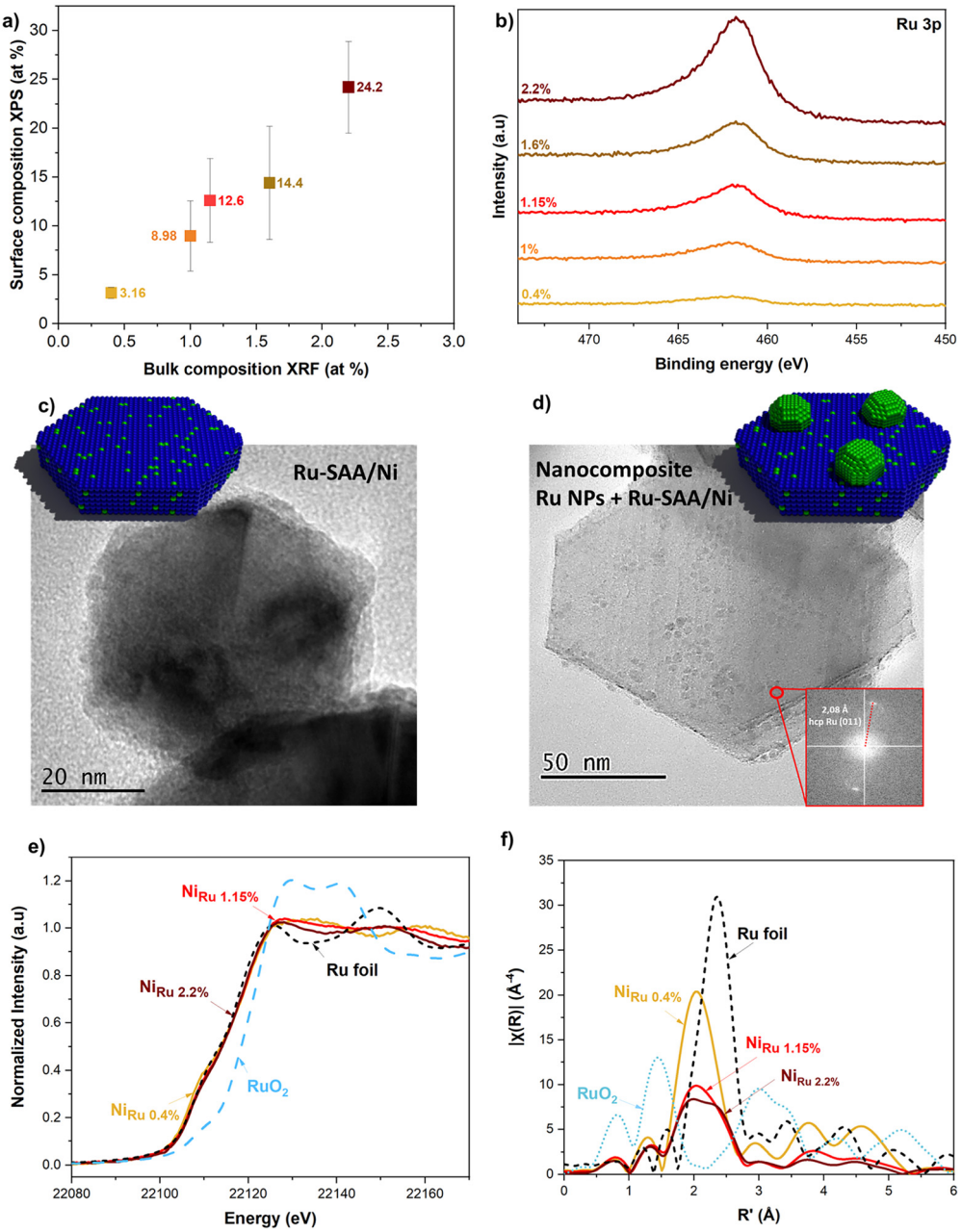

Fig. 2 (a) Ru surface content (Ru/(Ru + Ni))% determined by XPS as a function of the bulk Ru content measured by XRF. (b) XPS spectra in the Ru 3p region for samples containing 0.4 to 2.2 Ru at%. (c) TEM micrograph and representation of Ru-SAA/Ni particles containing 0.4 at% of Ru; (d) TEM micrograph of the composite material Ru-SAA/Ni + Ru nanoparticles containing 1 at% of Ru, with the corresponding FFT of the highlighted area showing the characteristic distances of the Ru hcp structure, and a 3D model of the catalyst. (e) XANES and (f) FT-EXAFS spectra at the Ru K-edge as a function of Ru% in the heterostructured particles.

ticles. Since the Ru 3d region overlaps with the C 1s signals, reliable fitting of the Ru 3d region is highly hazardous, especially at low Ru content; therefore, Ru XPS spectra were analyzed in the 3p region. The signal recorded for the sample containing 0.4% of Ru was too weak to be interpreted. For samples with 1 at% Ru sample and above, we observe a peak centered at *ca.* 461.8–461.9 eV with a full width at half maximum (FWHM) larger than 4 eV, indicating a mixture of both metallic and oxidized Ru species (Fig. 2b).[28] In addition, the spectra of Ru in the 3d and 3p regions were compared to those of commercial Ru/C particles to evidence modifications in the electronic environment of Ru in the composite material (see Fig. S2). In Ru/C materials, significantly weaker interactions are expected compared to those of the composite material.[29] A distinct shift of *ca.* 0.7 eV in the Ru 3d5/2 and Ru 3p peak positions in the composite materials towards lower

binding energy is clearly observed compared to commercial Ru/C. These results suggest a redistribution of electron density in Ru due to its interaction with the surrounding Ni atoms and possible modification of the electrochemical activity.

TEM, along with XANES and extended X-ray absorption fine structure (EXAFS) spectra, allowed us to obtain further insight into the different samples. The TEM images of $Ni_{Ru\ 0.4\%}$ (Fig. 2c) reveal the presence of aggregated hexagonal platelets, and the HRTEM images reveal crystalline planes corresponding to the Ni fcc (Fig. S3) and no noticeable presence of other types of particles. Energy dispersive X-ray (EDX) analysis confirms the presence of a very small amount of Ru, approximately 0.5%. The edge position of the Ru K-edge XANES spectrum of $Ni_{Ru\ 0.4\%}$ corresponds to that of the zero-valent Ru metallic foil (Fig. 2e). The FT-EXAFS spectra at the Ru K-edges were analyzed in the k^3-space, with EXAFS spectra and the corresponding fits shown in Fig. 2f and SI3, respectively. For $Ni_{Ru\ 0.4\%}$, a sharp peak centered at an apparent distance of R' = 2.05 Å is observed, which was fitted with a Ru–Ni shell lying at a real distance of R = 2.50 Å. This distance is consistent with what was observed in another work, where a similar characteristic sharp peak at an apparent distance of R' = 2.1 Å was assigned to Ru–Ni distances in a Ru single-atom alloy (SAA) dispersed in Ni particles containing 0.4 wt% Ru.[30] Here too, the low value of the Debye–Waller factor (σ^2 = 0.0036) obtained in our fits (see Table S1) reflects the presence of a single Ru–Ni interaction and confirms the single-atom alloy structure. This particular signal shape has been previously observed in SACs where heteroatoms are embedded in a carbon matrix.[9] The higher Ru content detected by XPS compared to XRF, the absence of Ru particles at the Ni surface, and the parameters determined from the EXAFS spectra for the $Ni_{Ru\ 0.4\%}$ material all suggest a SAA-type structure, where isolated Ru atoms are dispersed within a Ni matrix.

The TEM characterization of $Ni_{Ru\ 1\%}$ shows the same aggregated nanoplatelets observed in the previous sample, but with small nanoparticles (*ca.* 5 nm) decorating their surfaces (Fig. 2d). The Fast-Fourier transform (FFT) of the HRTEM images obtained from these small nanoparticles reveals interplanar distances of 2.38 and 2.08 Å, characteristic of the (010) and (011) planes of hexagonal closed packed (hcp) Ru, respectively. The EDX analysis of the sample indicates an average Ru content of 1.2%, in agreement with the XRF data. As the bulk Ru content in the material varies from 1 to 2.5 at%, the XANES spectra of the Ni_{Ru} particles at the Ru K-edge overlap and are slightly shifted to higher energies compared with the Ru foil (Fig. 2e), meaning that Ru is slightly more oxidized in the particles than in pure metal. The EXAFS spectra of the materials containing 1 at% Ru and above exhibit an additional peak compared to $Ni_{Ru\ 0.4\%}$, characteristic of Ru shell distances of 2.4 Å. The contribution of this second component increases with an increase in the Ru content in the material, confirming the presence of Ru nanoparticles, as previously observed *via* TEM for the $Ni_{Ru\ 1.1\%}$ sample. We observe two contributions in all the materials with Ru content higher than 0.4 at%: the peak characteristic of Ru–Ni distances and, an additional peak characteristic of Ru–Ru distances increases. This indicates that for Ru contents above 0.4 at%, Ru SAAs dispersed in a Ni matrix coexist with Ru nanoparticles to form a composite material.

At this point, we can conclude that the one-pot synthetic strategy results in the formation of Ru SAAs dispersed within Ni particles up to 0.4 Ru at% (Ru-SAA/Ni). When the Ru content exceeds this value, we obtain a composite material where Ru nanoparticles decorate the surface of Ru-SAA/Ni. The ratio of SAA to Ru nanoparticles in the composite material can be adjusted by varying the initial amount of the Ru precursor.

Electrochemical performance

The electrochemical activity of the prepared materials for the HER was therefore evaluated in a three-electrode electrochemical setup in 0.1 M KOH. The linear sweep voltammograms of these materials are shown in Fig. 3a. The comparisons of overpotentials measured at 10 mA cm^{-2}, Tafel slopes, and mass activities determined at −150 mV, normalized to the actual platinum group metal (PGM) loading, are presented in Fig. 3b–d. Pure Ni particles, prepared under similar conditions but without the addition of the Ru precursor, present a large overpotential of 293 mV *vs.* RHE at 10 mA cm^{-2}. The Ru-SAA/Ni catalyst ($Ni_{Ru\ 0.4\%}$) shows a much lower overpotential of 193 mV *vs.* RHE, although it is still higher than that of the state-of-the-art Pt, which has an overpotential of 109 mV *vs.* RHE at 10 mA cm^{-2}. When combining the SAA and Ru nanoparticles ($Ni_{Ru\ 1\%}$), the overpotential becomes comparable to that of commercial Pt/C but with a significantly lower noble metal loading and thus much higher mass activity (see Fig. 3d).

In order to demonstrate the unique synergetic effect in the composite material due to the close vicinity of atomically dispersed Ru atoms and Ru nanoparticles, the electrochemical performance of two different reference systems with similar Ru loadings was evaluated: pure Ni particles synthesized under the same conditions mixed with 2 at% Ru/C particles (Ni + 2% Ru NPs), and Ru-SAA Ni particles (*i.e.* the Ru-SAA Ni compound obtained in this work) mixed with 1 at% Ru/C particles ($Ni_{Ru\ 0.4}$ + 1% Ru NPs) (Fig. 3b and d and Fig. S4). The overpotential at 10 mA cm^{-2} of the (Ni + 2% Ru NPs) and ($Ni_{Ru\ 0.4}$ + 1% Ru NPs) are 150 and 145 mV, respectively, while it is 110 mV for the composite materials *i.e.* when Ru nanoparticles are deposited at the surface of Ru-SAA Ni particles ($Ni_{Ru\ 1.5\%}$). The larger overpotential and therefore lower mass activity of these two systems compared to the composite catalyst demonstrates that a close vicinity between the different active sites is needed for a synergetic effect and enhanced performance.

Another interesting observation is that as the NPs/SAA ratio increases further in the composite material, the performances do not vary significantly, and the Tafel slopes remain constant. This indicates that the reaction step occurring at the surface of the Ru nanoparticles is not the rate-determining step under these conditions. For more insight into the role of the different catalyst components, a computational study was carried out. To simulate the Ru SAA and NP deposited on Ni,

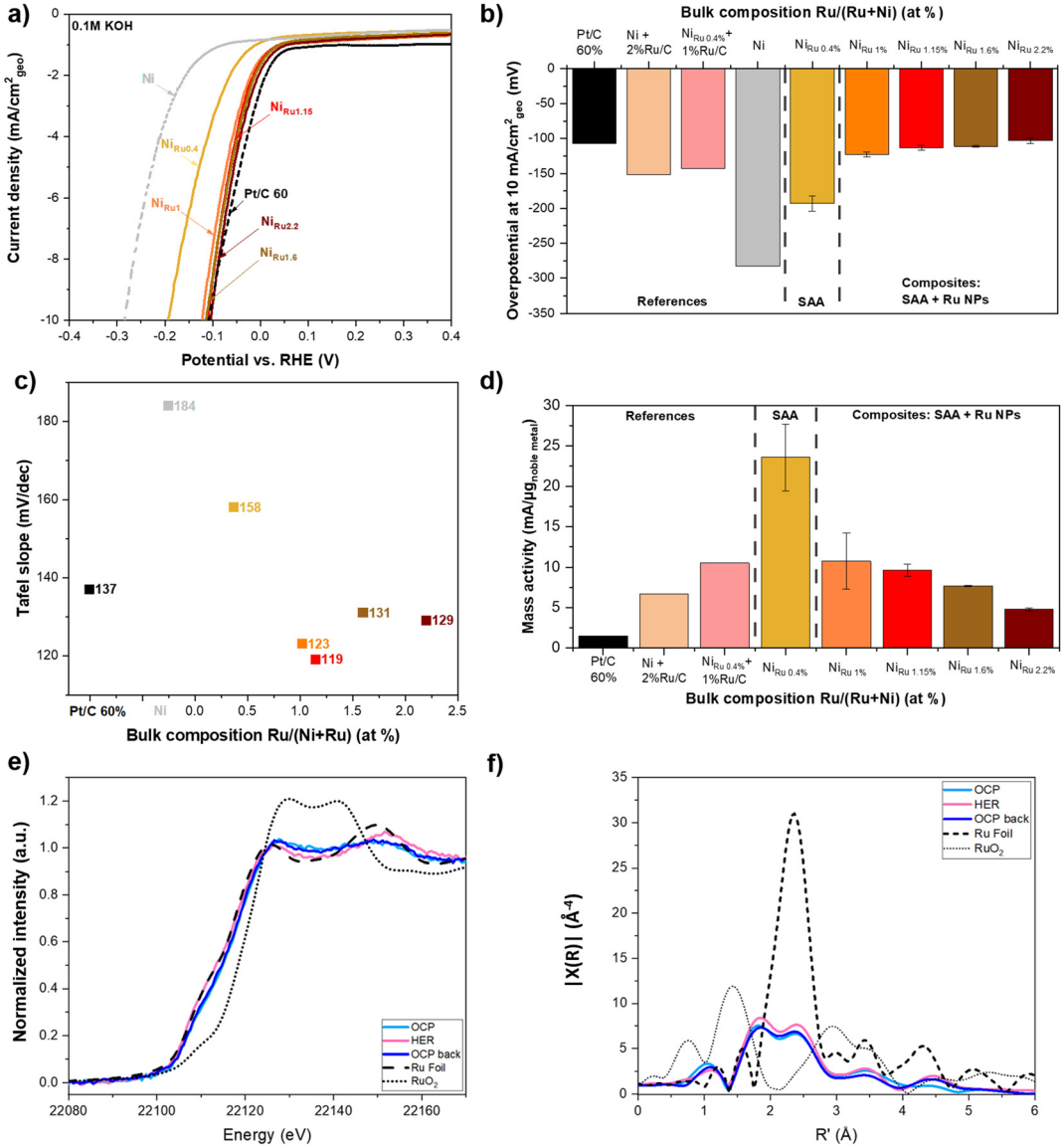

Fig. 3 (a) Linear sweep voltammetry of the Ni_{Ru} catalyst with varying Ru contents, compared with a commercial Pt/C catalyst. Measurements were performed in 0.1 M KOH (mass loading for each catalyst was 100 μg cm^{-2}); (b) overpotential at 10 mA cm^{-2} from the data in panel (a). (c) Tafel slopes of Ni_{Ru} catalysts compared to commercial Pt/C in alkaline media (0.1 M KOH), and (d) mass activity of PGM at −0.10 V of Ni_{Ru} catalysts compared to Pt/C and a catalyst mixture of Ni and 2 at% of Ru. (e) XANES and (f) EXAFS spectra at the Ru K-edge recorded under *operando* conditions at the OCP with the sample $Ni_{Ru\ 2.2}$, under HER conditions at −0.075 mV *vs.* RHE for 2 h and back to the OCP.

we studied single Ru atoms in a Ni(111) surface and a Ru cluster supported on Ni(111), respectively, as shown in Fig. 4a. Water dissociation is the first and possibly rate-limiting step in an alkaline HER. Therefore, the steps pertaining to water dissociation are studied over the catalyst surface of Ni, Ru and Ru–Ni (SAA and NP), in particular, for the adsorption of H_2O, OH* and H*. To mimic alkaline conditions and explicitly account for the effect of the electrochemical potential, including on transition states,[31] grand canonical DFT (GC-DFT) in combination with an implicit KOH electrolyte (VASPSol++)[25] is applied, in close analogy to previous studies on the HER[32] and nickel-based catalysts.[33,34]

Under alkaline conditions, OH^- ions are abundant and might strongly adsorb on some surface sites. Fig. S5 and Fig. 4b show the adsorption energy (ΔE) and free energy (ΔG) of OH adsorption for different surface sites. Apart from the $Ni–Ru_{NP}$, all other surfaces exhibit a mild and reversible OH* adsorption. As the Ru-NP features Ru atoms with low coordination numbers (CN), its top sites (CN 5) adsorb OH* strongly with an adsorption energy of −0.74 to −0.88 eV (Fig. S6). This strong interaction suggests that these sites will be covered by spectator OH* and, thus, do not play a role during catalytic water dissociation. These spectator OH* species are likely to contribute to the partially oxidized Ru signal observed in

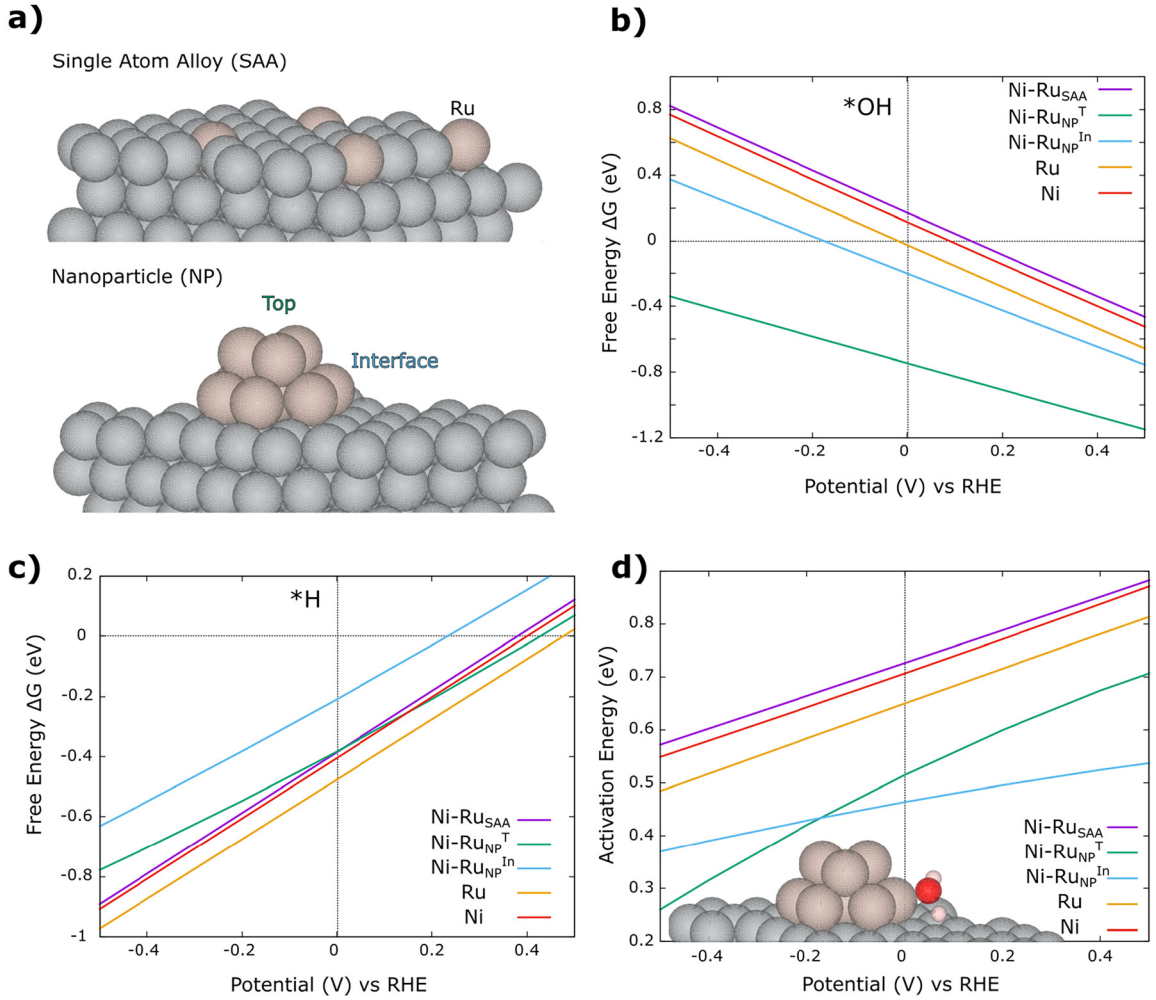

Fig. 4 (a) Side view of the Ni–Ru-SAA and Ni–Ru-NP structures; Ni (grey) and Ru (orange). (b and c) Electrochemical potential-dependent Gibbs energies of adsorbed OH* (b) and H* (c) on different surfaces. (d) Activation energy of H–OH dissociation on all surfaces; inset: structure of the water dissociation transition state at the Ni–Ru-NP interfacial site.

XANES (*vide supra*). However, the Ni–Ru$_{NP}$ interfacial sites show a weaker OH* and H* adsorption compared to the top site and can effectively participate in catalytic water dissociation.

At negative potentials, the free energy of H_2O* adsorption is weakly unfavorable on all surfaces, with Ni–Ru$_{SAA}$ and Ni–Ru$_{NP}$ being the most favorable (see Fig. S6). After H_2O* adsorption, the molecule dissociates, and H* adsorbs on the surface. Thermodynamically, H* adsorption is favorable on all surfaces, and a ΔG close to 0 facilitates subsequent Heyrovsky/Tafel steps. Compared to Ni and Ru surfaces, Ni–Ru$_{SAA}$ and Ni–Ru$_{NP}$-Top bind H* less strongly. Interestingly, it is the Ni–Ru$_{NP}$-interface site that binds H* the least strongly (but still exergonic), suggesting that these sites should have the highest catalytic activity. Nevertheless, these "interface" H* might diffuse to the Ni surface (spill-over effect), where they are more strongly adsorbed. After water dissociation, OH* needs to desorb from the surface to not cover and poison the catalyst. The Ni–Ru$_{SAA}$ catalyst shows the least preferred OH* adsorption, suggesting that the active site can be easily regenerated following the HER. In contrast, Ru and Ni–Ru$_{NP}$ surfaces show a stronger OH* adsorption, which can slow down the regeneration of the catalyst. However, H* (a precursor for the Heyrovsky/Tafel step) and OH* show comparable overbinding on the Ni–Ru$_{NP}$-interface site (−0.21 eV for H* and −0.20 eV for OH*), suggesting that either of the steps might be limiting. This slow regeneration is counter-balanced by the water dissociation step that is uniquely favorable at the Ni–Ru$_{NP}$ interface site (Fig. 4d, Table S2), with OH* adsorbing on the Ru$_{NP}$ and H* adsorbing on the Ni surface near the Ru$_{NP}$.

The kinetics of water dissociation are governed by the transition state energy of the H–OH bond-breaking step. The potential dependence of the H–OH transition state (Fig. 4d) for Ni, Ru, and Ni–Ru$_{SAA}$ shows a slope of roughly 0.5 eV/V with minor differences, implying that the kinetic barrier and mechanism of this Volmer step are similar for these surfaces. However, for the Ni–Ru$_{NP}$ surfaces, there is a reduction in the activation energy, with the lowest barrier (~0.45 eV) for Ni–Ru$_{NP}$-interface, implying a significantly faster reaction. In

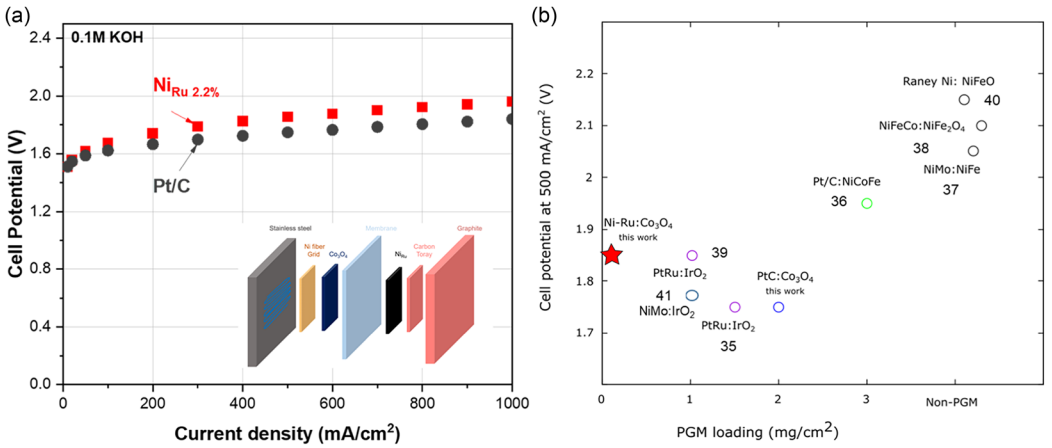

Fig. 5 (a) Polarization curves of MEAs recorded in 0.1 M KOH at 50 °C, prepared with a Co_3O_4 anode catalyst and a PiperION 40 μm-thick membrane, with a noble metal loading of 0.11 mg cm^{-2} of Ru (5 mg of $Ni_{Ru\ 2.2}$ at%; squares) or 2 mg cm^{-2} of Pt (commercial Pt/C; circles) at the cathode. (b) Cell potential measured at 0.5 A cm^{-2} in this work compared to values reported in the literature using a similar electrolyte concentration of 0.1 M KOH. Cited references: Pt/C/Co_3O_4;[35] Pt/C/IrO_2;[36] Pt/C/NiFeCo;[37] NiMo/NiFe;[38] NiFeCo/$NiFe_2O_4$;[39] PtRu/IrO_2,[40] RaneyNi/NiFeO,[41] and NiMo/IrO_2.[42]

summary, GC-DFT supports the activating effect of Ru-SAA by making the OH* desorption step slightly more favorable, while leaving the thermodynamics of H* and the kinetics of water dissociation nearly unchanged. In contrast, OH* binds more strongly to the Ru-NP. This strong OH* binding yields spectator OH* on the one hand but significantly facilitates the water dissociation step on the other hand, with H* being adsorbed on the activated Ni surface and OH* being reversibly adsorbed at the Ru side of the interface. The considerably lower activation energy for water activation at the Ru/Ni interface is compatible with the experimentally observed kinetic pattern: having Ru-NPs improves the kinetics, but having "more" of them has only a negligible effect, since water activation is no longer the limiting step.

XAS *operando* experiments were performed to assess the catalyst stability under HER conditions according to the following steps: open circuit potential (OCP), hold at −0.075 mV *vs.* RHE for 2 h and back to OCP conditions. On the XANES spectra recorded at the Ru edge for the sample $Ni_{Ru\ 2.2\%}$, we observe a slight shift of 2 eV (measured at the half-edge jump, where intensity = 0.5) towards low energies, indicating a decrease in the Ru average oxidation state towards a fully metallic species. The initial edge position (and therefore oxidation state) is recovered when the material comes back to open circuit conditions. No significant changes in the EXAFS spectra are observed after 2 h under HER conditions, which shows that the material and, in particular, the distribution of Ru atoms in both single-site positions and as nanoparticles remain stable under operating conditions.

The catalysts were further tested in AEM single cells at 50 °C using 0.1 M KOH as the electrolyte. The polarization curves of the MEAs prepared with either the commercial Pt/C or $Ni_{Ru\ 2.2\%}$ catalyst at the cathode, tested using the PiperION 40 μm membrane and standard baseline Co_3O_4 nanoparticles as an anode catalyst,[35] are presented in Fig. 5a. The cell potential measured at 0.5 A cm^{-2} is 1.75 V with 2 mg cm^{-2} Pt and 1.85 V with the $Ni_{Ru\ 2.2\%}$ catalyst (5 mg cm^{-2} total metal loading), and 1.93 and 1.95 V at 1 A cm^{-2}, respectively. In other words, with only 0.1 mg cm^{-2} of noble metal, the MEA prepared using the $Ni_{Ru\ 2.2\%}$ composite catalyst exhibits a very similar performance compared to that prepared with 2 mg cm^{-2} of Pt. In Fig. 5b, a comparison of cell potentials at 500 mA cm^{-2} reported in the literature and measured in 0.1 M KOH with Ni_{Ru} samples is displayed. Although very few publications report electrochemical data in 0.1 M KOH, these results highlight the competitive performance of the $Ni_{Ru\ 2.2\%}$ catalyst prepared in this work.

Conclusion

We prepared Ru single-atom alloys (Ru-SAA) dispersed within Ni nanoparticles using a one-step, scalable synthesis method. We demonstrate that a Ru-SAA forms within a nickel matrix, up to a noble metal content of 0.4 at% Ru, exhibiting a higher efficiency compared with their pure Ni counterparts. Higher Ru contents result in composite materials with Ru nanoparticles on Ru-SAA/Ni supports, with electrochemical performances comparable to those achieved using commercial Pt/C with only 5% of the noble metal loading. Comprehensive characterizations, including XPS, XAS and TEM, confirm the distinct structures and synergetic interactions between Ru-SAA/Ni and Ru nanoparticles, including under operating conditions. According to our computational insight, the Ru/Ni interface is particularly apt for activating water. Moreover, AEM single-cell tests in low-concentration KOH highlight the competitive efficiency of Ni_{Ru} composites compared with commercial catalysts made of pure noble metals, achieving high current densities with minimal Ru usage, making this catalyst a promising candidate for integration into commercial-scale electrolyzers. These findings validate our synthetic strategy and provide valuable insights for catalyst design, supporting

efforts to provide cost-effective, high-performance solutions for sustainable hydrogen production under alkaline conditions. Our current research in this direction focuses on optimizing the architecture of the catalyst, as well as the ionomer/catalyst and carbon/catalyst ratios, for long-term testing in AEMWEs.

Author contributions

GK, MSDF, SB, LL, CM, FD, MK, MCH performed the investigation, AZ, SNS, SWB, CT, BLK supervised and validated the different aspects of the work; MG and JP conceptualized and managed the project, JP wrote the publication, and all the co-authors reviewed and edited the paper.

Conflicts of interest

There are no conflicts to declare.

Data availability

All data supporting the findings of this study are provided in the supplementary information (SI). Supplementary information: electrochemical measurements, physicochemical characterization of all the materials presented in the current paper and additional calculations. See DOI: https://doi.org/10.1039/d6nr00391e.

Additional datasets, including raw experimental files and microscopy images, are available from the corresponding author upon reasonable request.

Acknowledgements

The authors acknowledge financial support from the ANR (Hykalin ANR-21-CE05-0017), the Region Ile de France through the DIM-MaTeRe for the 2024 travel allocation. The XAS experiments were performed on the SAMBA beamline at Synchrotron Soleil (Proposal 2022 1334). We sincerely acknowledge Marco Faustini and Cédric Boissière for the fruitful discussions. We acknowledge the ITODYS CARISMA and MATRIX platforms (Université Paris Cité, CNRS UMR 7086, Paris, France) and Sophie Nowak and Ivonne Cocca for EDXRF and Philippe Decorse for the XPS measurements. The electrolyzer and electrochemical testing work at UC Berkeley was supported by the U.S. Department of Energy (DOE), Office of Energy Efficiency and Renewable Energy, under award DE-EE0011322. We acknowledge support from the CBPsmn (PSMN, Pôle Scientifique de Modélisation Numérique) of the ENS de Lyon for the computing resources. The platform operates the SIDUS solution.[43]

References

1 N. Du, C. Roy, R. Peach, M. Turnbull, S. Thiele and C. Bock, Anion-Exchange Membrane Water Electrolyzers, *Chem. Rev.*, 2022, **122**(13), 11830–11895.
2 D. Hua, J. Huang, E. Fabbri, M. Rafique and B. Song, Development of Anion Exchange Membrane Water Electrolysis and the Associated Challenges: A Review, *ChemElectroChem*, 2023, **10**(1), e202200999.
3 G. Lindquist and S. Boettcher, Reports From The Frontier: Overcoming Limitations for Pure-water Anion-exchange-membrane Electrolysis, *Electrochem. Soc. Interface*, 2023, **32**(2), 32.
4 Y. Zhu, L. Li, H. Cheng and J. Ma, Alkaline Hydrogen Evolution Reaction Electrocatalysts for Anion Exchange Membrane Water Electrolyzers: Progress and Perspective, *JACS Au*, 2024, **4**(12), 4639–4654.
5 M. Lao, P. Li, Y. Jiang, H. Pan, S. X. Dou and W. Sun, From fundamentals and theories to heterostructured electrocatalyst design: An in-depth understanding of alkaline hydrogen evolution reaction, *Nano Energy*, 2022, **98**, 107231.
6 J. Wei, M. Zhou, A. Long, Y. Xue, H. Liao, C. Wei and Z. J. Xu, Heterostructured Electrocatalysts for Hydrogen Evolution Reaction Under Alkaline Conditions, *Nano-Micro Lett.*, 2018, **10**(4), 75.
7 R. Subbaraman, D. Tripkovic, D. Strmcnik, K.-C. Chang, M. Uchimura, A. P. Paulikas, V. Stamenkovic and N. M. Markovic, Enhancing Hydrogen Evolution Activity in Water Splitting by Tailoring Li^+-$Ni(OH)_2$-Pt Interfaces, *Science*, 2011, **334**(6060), 1256–1260.
8 Y. Yang, Y. Yu, J. Li, Q. Chen, Y. Du, P. Rao, R. Li, C. Jia, Z. Kang, P. Deng, Y. Shen and X. Tian, Engineering Ruthenium-Based Electrocatalysts for Effective Hydrogen Evolution Reaction, *Nano-Micro Lett.*, 2021, **13**(1), 160.
9 P. Serp, Synergy Between Supported Metal Single Atoms and Nanoparticles and their Relevance in Catalysis, *ChemCatChem*, 2023, **15**(15), e202300545.
10 H. Ou, D. Wang and Y. Li, How to select effective electrocatalysts: Nano or single atom?, *Nano Sel.*, 2021, **2**(3), 492–511.
11 (*a*) P. Su, W. Pei, X. Wang, Y. Ma, Q. Jiang, J. Liang, S. Zhou, J. Zhao, J. Liu and G. Q. Lu, Exceptional Electrochemical HER Performance with Enhanced Electron Transfer between Ru Nanoparticles and Single Atoms Dispersed on a Carbon Substrate, *Angew. Chem., Int. Ed.*, 2021, **60**(29), 16044–16050; (*b*) Q. Wu, H. Li, Y. Zhou, S. Lv, T. Chen, S. Liu, W. Li and Z. Chen, Convenient Synthesis of a Ru Catalyst Containing Single Atoms and Nanoparticles on Nitrogen-Doped Carbon with Superior Hydrogen Evolution Reaction Activity in a Wide pH Range, *Inorg. Chem.*, 2022, **61**(28), 11011–11021.
12 (*a*) Y. Zhu, K. Fan, C.-S. Hsu, G. Chen, C. Chen, T. Liu, Z. Lin, S. She, L. Li, H. Zhou, Y. Zhu, H. M. Chen and H. Huang, Supported Ruthenium Single-Atom and Clustered Catalysts Outperform Benchmark Pt for Alkaline Hydrogen Evolution, *Adv. Mater.*, 2023, **35**(35), 2301133;

(*b*) J. Zhang, Y. Gu, Y. Lu, C. Zhu, G. Liu, C. Wang, D. Sun, Y. Tang and H. Sun, Each performs its own functions: Nickel oxide supported ruthenium single-atoms and nanoclusters relay catalysis with multi-active sites for efficient alkaline hydrogen evolution reaction, *Appl. Catal., B*, 2023, **325**, 122316; (*c*) F. Li, Q. Wu, W. Yuan and Z. Chen, Ruthenium-based single atom catalysts: synthesis and application in the electrocatalytic hydrogen evolution reaction, *Dalton Trans.*, 2024, **53**(29), 12022–12033.

13 Z. Xiaoxiang, G. Yuxuan and W. Congwei, Multi-interface engineering of nickel-based electrocatalysts for alkaline hydrogen evolution reaction, *Energy Mater.*, 2024, **4**(4), 400044.

14 L. Huo, C. Jin, K. Jiang, Q. Bao, Z. Hu and J. Chu, Applications of Nickel-Based Electrocatalysts for Hydrogen Evolution Reaction, *Adv. Energy Sustainability Res.*, 2022, **3**(4), 2100189.

15 K. Chen, Z. Liu, S. Zhu, Y. Liu, Y. Liu, L. Wang, T. Xia, Z. Zhao, H. Gao, S. Cheng and H. Guo, Ruthenium–Nickel Nanoparticles with Unconventional Face-Centered Cubic Crystal Phase for Highly Active Electrocatalytic Hydrogen Evolution, *Adv. Funct. Mater.*, 2024, **34**(44), 2406259.

16 J. Xia, M. Volokh, G. Peng, Y. Fu, X. Wang and M. Shalom, Low-Cost Porous Ruthenium Layer Deposited on Nickel Foam as a Highly Active Universal-pH Electrocatalyst for the Hydrogen Evolution Reaction, *ChemSusChem*, 2019, **12**(12), 2780–2787.

17 S. Ruck, A. Hutzler, S. Thiele and C. van Pham, Highly Active NiRu/C Cathode Catalyst Synthesized by Displacement Reaction for Anion Exchange Membrane Water Electrolysis, *Small Methods*, 2025, 2401179.

18 O. van der Heijden, S. Park, R. E. Vos, J. J. J. Eggebeen and M. T. M. Koper, Tafel Slope Plot as a Tool to Analyze Electrocatalytic Reactions, *ACS Energy Lett.*, 2024, **9**(4), 1871–1879.

19 J. J. Rehr, J. J. Kas, F. D. Vila, M. P. Prange and K. Jorissen, Parameter-free calculations of X-ray spectra with FEFF9, *Phys. Chem. Chem. Phys.*, 2010, **12**(21), 5503–5513.

20 Q. Zhao and H. J. Kulik, Where Does the Density Localize in the Solid State? Divergent Behavior for Hybrids and DFT+U, *J. Chem. Theory Comput.*, 2018, **14**(2), 670–683.

21 G. Kresse and J. Furthmüller, Efficient iterative schemes for ab initio total-energy calculations using a plane-wave basis set, *Phys. Rev. B: Condens. Matter Mater. Phys.*, 1996, **54**(16), 11169–11186.

22 P. E. Blöchl, Projector augmented-wave method, *Phys. Rev. B: Condens. Matter Mater. Phys.*, 1994, **50**(24), 17953–17979.

23 J. P. Perdew, K. Burke and M. Ernzerhof, Generalized Gradient Approximation Made Simple, *Phys. Rev. Lett.*, 1996, **77**(18), 3865–3868.

24 S. N. Steinmann, G. Csonka and C. Corminboeuf, Unified Inter- and Intramolecular Dispersion Correction Formula for Generalized Gradient Approximation Density Functional Theory, *J. Chem. Theory Comput.*, 2009, **5**(11), 2950–2958.

25 S. M. R. Islam, F. Khezeli, S. Ringe and C. Plaisance, An implicit electrolyte model for plane wave density functional theory exhibiting nonlinear response and a nonlocal cavity definition, *J. Chem. Phys.*, 2023, **159**(23), 234117.

26 (*a*) F. Fievet, S. Ammar-Merah, R. Brayner, F. Chau, M. Giraud, F. Mammeri, J. Peron, J. Y. Piquemal, L. Sicard and G. Viau, The polyol process: a unique method for easy access to metal nanoparticles with tailored sizes, shapes and compositions, *Chem. Soc. Rev.*, 2018, **47**, 5187–5233; (*b*) R. K. Ramamoorthy, A. Viola, B. Grindi, J. Peron, C. Gatel, M. Hytch, R. Arenal, L. Sicard, M. Giraud, J.-Y. Piquemal and G. Viau, One-Pot Seed-Mediated Growth of Co Nanoparticles by the Polyol Process: Unraveling the Heterogeneous Nucleation, *Nano Lett.*, 2019, **19**(12), 9160–9169.

27 S. Tanuma, C. J. Powell and D. R. Penn, Calculations of electron inelastic mean free paths. IX. Data for 41 elemental solids over the 50 eV to 30 keV range, *Surf. Interface Anal.*, 2011, **43**(3), 689–713.

28 D. J. Morgan, Resolving ruthenium: XPS studies of common ruthenium materials, *Surf. Interface Anal.*, 2015, **47**(11), 1072–1079.

29 M. Smiljanic, M. Bele, L. Pavko, A. Hrnjic, F. Ruiz-Zepeda, L. Bijelic, A. R. Kamsek, M. Nuhanovic, A. Marsel, L. Gasparic, A. Kokalj and N. Hodnik, Titanium oxynitride-supported Ru nanoparticles as exceptional electrocatatlysts for alkaline hydrogen evolution reaction, *Chem. Eng. J.*, 2025, **517**, 164204–164219.

30 W. Liu, H. Feng, Y. Yang, Y. Niu, L. Wang, P. Yin, S. Hong, B. Zhang, X. Zhang and M. Wei, Highly-efficient RuNi single-atom alloy catalysts toward chemoselective hydrogenation of nitroarenes, *Nat. Commun.*, 2022, **13**(1), 3188.

31 N. Abidi and S. N. Steinmann, How are transition states modeled in heterogeneous electrocatalysis?, *Curr. Opin. Electrochem.*, 2022, **33**, 100940.

32 N. Abidi, A. Sahu, P. Raybaud and S. N. Steinmann, Electrochemical Potential-Dependent Stability and Activity of MoS3 during the Hydrogen Evolution Reaction, *ACS Catal.*, 2023, **13**(23), 15290–15300.

33 S. N. Steinmann, C. Michel, R. Schwiedernoch, M. Wu and P. Sautet, Electro-carboxylation of butadiene and ethene over Pt and Ni catalysts, *J. Catal.*, 2016, **343**, 240–247.

34 L. Treps, T. Ermacora, A. Giacomelli, C. Michel and S. N. Steinmann, Surface state of NiOOH under oxidative conditions: Can dopants induce surface oxidation?, *Electrochim. Acta*, 2025, **524**, 145960.

35 R. A. Krivina, G. A. Lindquist, S. R. Beaudoin, T. N. Stovall, W. L. Thompson, L. P. Twight, D. Marsh, J. Grzyb, K. Fabrizio, J. E. Hutchison and S. W. Boettcher, Anode Catalysts in Anion-Exchange-Membrane Electrolysis without Supporting Electrolyte: Conductivity, Dynamics, and Ionomer Degradation, *Adv. Mater.*, 2022, **34**(35), 2203033.

36 S. Koch, P. A. Heizmann, S. K. Kilian, B. Britton, S. Holdcroft, M. Breitwieser and S. Vierrath, The effect of ionomer content in catalyst layers in anion-exchange mem-

brane water electrolyzers prepared with reinforced membranes (Aemion+™), *J. Mater. Chem. A*, 2021, **9**(28), 15744–15754.

37 K. Yue, J. Liu, Y. Zhu, C. Xia, P. Wang, J. Zhang, Y. Kong, X. Wang, Y. Yan and B. Y. Xia, In situ ion-exchange preparation and topological transformation of trimetal–organic frameworks for efficient electrocatalytic water oxidation, *Energy Environ. Sci.*, 2021, **14**(12), 6546–6553.

38 S. Campagna Zignani, M. L. Faro, A. Carbone, C. Italiano, S. Trocino, G. Monforte and A. S. Aricò, Performance and stability of a critical raw materials-free anion exchange membrane electrolysis cell, *Electrochim. Acta*, 2022, **413**, 140078.

39 I. V. Pushkareva, A. S. Pushkarev, S. A. Grigoriev, P. Modisha and D. G. Bessarabov, Comparative study of anion exchange membranes for low-cost water electrolysis, *Int. J. Hydrogen Energy*, 2020, **45**(49), 26070–26079.

40 J. Liu, Z. Kang, D. Li, M. Pak, S. M. Alia, C. Fujimoto, G. Bender, Y. S. Kim and A. Z. Weber, Elucidating the Role of Hydroxide Electrolyte on Anion-Exchange-Membrane Water Electrolyzer Performance, *J. Electrochem. Soc.*, 2021, **168**(5), 054522.

41 B. Motealleh, Z. Liu, R. I. Masel, J. P. Sculley, Z. Richard Ni and L. Meroueh, Next-generation anion exchange membrane water electrolyzers operating for commercially relevant lifetimes, *Int. J. Hydrogen Energy*, 2021, **46**(5), 3379–3386.

42 A. Shirwalkar, M. Kaur, S. Zhong, M. Pupucevski, K. Hu, Y. Yan, J. Lattimer and J. McKone, Comparing Intrinsic Catalytic Activity and Practical Performance of Ni-and Pt-Based Alkaline Anion Exchange Membrane Water Electrolyzer Cathodes, *ACS Energy Lett.*, 2025, **10**, 1779–1785.

43 E. Quemener and M. Corvellec, SIDUS—the solution for extreme deduplication of an operating system, *Linux J.*, 2013, **2013**(235), 3.